Original article

Nuclear Medicine Communications

Truncation correction of fan beam transmission data for attenuation correction using parallel beam emission data on a 3-detector SPECT system

Yasuyuki Takahashi[a], Kenya Murase[a], Teruhito Mochizuki[b], Hiroshi Higashino[c] and Nobutoku Motomura[d]

Background When the simultaneous transmission computed tomography (TCT)/single photon emission CT (SPECT) acquisition protocol is applied to myocardial studies using a 3-detector SPECT, the narrow effective field of view of a fan beam collimator used for TCT acquisition may cause truncation artifacts on TCT images. In this paper, we propose a new method of correcting for the truncation of TCT.

Methods The truncated parts of the TCT projection data are corrected using quadratic functions, based on the properties that the integral of non-truncated TCT projection data is constant at any projection angle and the position of the centre of gravity is focused on a fixed point. The usefulness of our method was investigated in phantom and human studies using a 3-detector SPECT equipped with one cardiac fan beam collimator for TCT and two parallel beam collimators for SPECT. We used ^{201}Tl as a tracer for SPECT and ^{99m}Tc as an external source for TCT.

Results The phantom and human studies showed that our method can adequately correct for the truncation of TCT data acquired using a fan beam collimator in a 3-detector SPECT, as long as there is no truncation in SPECT data.

Conclusion Our method appears to be useful for improving the SPECT images obtained using simultaneous TCT/SPECT acquisition in a 3-detector SPECT. However, further studies will be necessary to establish the clinical usefulness of this method. *Nucl Med Commun* 25:623–630

Nuclear Medicine Communications 2004, 25:623–630

Keywords: transmission computed tomography (TCT), single photon emission computed tomography (SPECT), truncation correction, 3-detector SPECT

[a]Department of Medical Engineering, Division of Allied Health Sciences, Osaka University Graduate School of Medicine, [b]Department of Radiology, Ehime University School of Medicine, [c]Department of Radiology, Ehime Prefectural Imabari Hospital and [d]Toshiba Medical Engineering Laboratory, Japan.

Correspondence to Yasuyuki Takahashi PhD, Department of Health, Health Planning Division, Ehime Prefectural Matsuyama Regional Office, 132, Kita-mochida, Matsuyama, Ehime, 790-8502 Japan.
Tel: +81 89 941 1111; fax: +81 89 931 8455;
e-mail: takahashi-yasuyuki@pref.ehime.jp

Received 26 February 2003 Revised 2 October 2003
Accepted 6 October 2003

Introduction

Radionuclides used for myocardial scintigraphy, such as ^{201}Tl and ^{99m}Tc, have relatively low photon energies, and their attenuation increases in deeper areas of the body. Therefore, the low radionuclide counts due to attenuation in the myocardial inferior wall in men and in the anterior wall in women with large breasts are known to result in a misdiagnosis of a hypoperfused area. To prevent misdiagnosis, accurate correction for attenuation is required.

Recently, attenuation correction has been performed using attenuation coefficient maps obtained by transmission computed tomography (TCT) in each patient [1,2]. However, the TCT method using a cardiac fan beam collimator with high sensitivity and resolution in deep areas [3] is not as common as the TCT for cerebral blood flow single photon emission computed tomography (SPECT), because there are problems such as the artifacts caused by the truncation of projection data outside the effective field of view (FOV) [4,5].

The purpose of this study was to propose a new method of correcting for truncation artifacts in TCT data acquired using a fan beam collimator for attenuation correction in a 3-detector SPECT, and to investigate the usefulness of this method using phantom and human studies.

Materials and methods

Truncation correction method

Given transmission and reference (blank) data for the slice, we define the projections $P(x,\theta)$ for bin x at angle θ as [6]

$$P(x,\theta) \equiv \ln\left(\frac{I_0(x,\theta)}{I(x,\theta)}\right), \qquad (1)$$

where $I_0(x,\theta)$ is the measured reference (blank) intensity for bin x at angle θ, and $I(x,\theta)$ is the measured

0143-3636 © 2004 Lippincott Williams & Wilkins

DOI: 10.1097/01.mnm.0000126515.49706.26

transmission intensity for bin x at angle θ. $I(x,\theta)$ is given by

$$I(x,\theta) = I_0(x,\theta)\exp\left(-\int \mu \mathrm{d}l_{x,\theta}\right), \quad (2)$$

where μ is the linear attenuation coefficient and $l_{x,\theta}$ denotes the projection ray path for bin x at angle θ. Then, the total projection sum for angle θ ($P_{\theta,tot}$) is given by

$$P_{\theta,tot} \equiv \sum_x P(x,\theta) = \sum_x \int \mu \mathrm{d}l_{x,\theta}. \quad (3)$$

Therefore, for non-truncated parallel beam projections, $P_{\theta,tot}$ is constant regardless of projection angle θ [6].

Furthermore, the position of the centre of gravity of non-truncated projections is focused on a fixed point; that is, the following equation is satisfied [7]:

$$\frac{\sum_x xP(x,\theta)}{\sum_x P(x,\theta)} = A\sin(\theta+\theta_c), \quad (4)$$

where A and θ_c are constants.

Based on the above two properties of non-truncated projections, we performed truncation correction for TCT as follows. After the fan beam to parallel beam transformation of truncated TCT projection data, the outline of the body was first extracted from non-truncated SPECT data. For doing so, a count threshold was applied to the sinogram of the SPECT data, and the body outline was delineated by the filtered back-projection (FBP) method [8] and was approximated by the 7th order Fourier series.

Second, the truncated projection data at angle θ [$P(x,\theta)$] were approximated by two elliptical functions, $f_l(x,\theta)$ and $f_r(x,\theta)$. The function $f_l(x,\theta)$ was obtained from two edge points of the body outline extracted above and the left edge point of the truncated projection data as illustrated by the solid line in Fig. 1(a), and $f_r(x,\theta)$ was obtained from two edge points of the body outline extracted above and the right edge point of the truncated projection data as illustrated by the solid line in Fig. 1(b).

Finally, the truncated parts of the projection data at angle θ were approximated by quadratic functions $g_l(x,\theta)$ and $g_r(x,\theta)$ as illustrated by dotted lines in Fig. 1. The functions $g_l(x,\theta)$ and $g_r(x,\theta)$ were given by

$$g_l(x,\theta) = a_0 + a_1x + a_2x^2 \quad (5)$$

and

$$g_r(x,\theta) = b_0 + b_1x + b_2x^2, \quad (6)$$

where a_0, a_1, a_2, b_0, b_1 and b_2 are constants, and these functions satisfy the following conditions

$$\begin{cases} g_l(x_0,\theta) = 0 \\ g_l(x_1,\theta) = y_1 \\ g_r(x_2,\theta) = y_2 \\ g_r(x_3,\theta) = 0 \end{cases} \quad (7)$$

Furthermore, from the two properties of non-truncated projection data mentioned above, we obtained the following equations:

$$\begin{aligned} &\left\{\int_{x_0}^{x_1} f_l(x,\theta)\mathrm{d}x + \int_{x_1}^{x_2} P(x,\theta)\mathrm{d}x + \int_{x_2}^{x_3} f_r(x,\theta)\mathrm{d}x\right. \\ &= \int_{x_0}^{x_1} g_l(x,\theta)\mathrm{d}x + \int_{x_1}^{x_2} P(x,\theta)\mathrm{d}x + \int_{x_2}^{x_3} g_r(x,\theta)\mathrm{d}x, \end{aligned}$$

Fig. 1

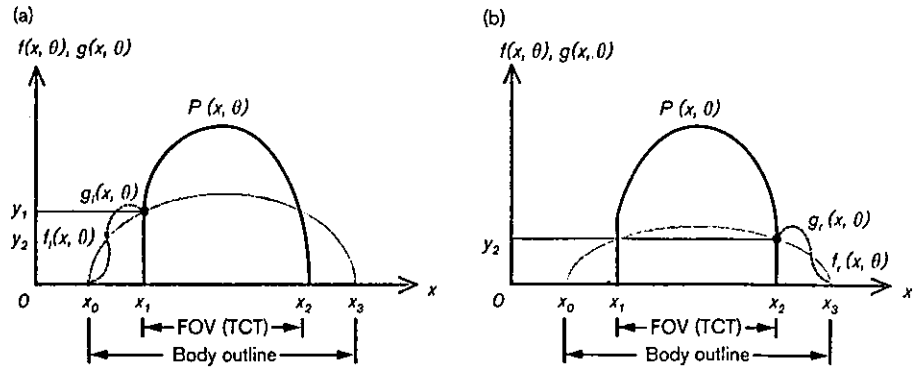

Illustration of the truncation correction method. The details are in the text. FOV, field of view; TCT, transmission computed tomography.

$$\left\{\int_{x_0}^{x_1} xf_l(x,\theta)\mathrm{d}x + \int_{x_1}^{x_2} xP(x,\theta)\mathrm{d}x + \int_{x_2}^{x_3} xf_r(x,\theta)\mathrm{d}x\right.$$
$$= \int_{x_0}^{x_1} xg_l(x,\theta)\mathrm{d}x + \int_{x_1}^{x_2} xP(x,\theta)\mathrm{d}x + \int_{x_2}^{x_3} xg_r(x,\theta)\mathrm{d}x. \quad (8)$$

Therefore, the constants a_0, a_1, a_2, b_0, b_1 and b_2 can be obtained by solving Equations 7 and 8, indicating that the truncated parts of projection data can be corrected using $g_l(x,\theta)$ and $g_r(x,\theta)$.

Phantom and human studies

SPECT system

The SPECT system used was GCA-9300A/UI (Toshiba Medical Systems, Tochigi, Japan) equipped with one cardiac fan beam collimator and two parallel beam collimators. The focal length, radial distance and FOV of the cardiac fan beam collimator were 802.3 mm, 225 mm and 241.3 mm, respectively. The radial distance and FOV of the parallel beam collimator were the same as those of the fan beam collimator. The TCT data were acquired using an external ^{99m}Tc gamma ray source, which was a sheet made from bellow tubes filled with 740 MBq of ^{99m}Tc. The tube was 1 mm in inner diameter, made of fluorocarbon resin embedded in an acrylic rectangular board of 250 × 100 mm. The SPECT system and external source are schematically illustrated in Fig. 2. As described later, the SPECT data were acquired using ^{201}TlCl. Therefore, for attenuation correction, it was necessary to convert the attenuation coefficient for ^{99m}Tc to that for ^{201}Tl. Since the attenuation coefficients for water at the ^{201}Tl (74 keV) and ^{99m}Tc (140 keV) energies are 0.184 cm^{-1} and 0.153 cm^{-1}, respectively, and the ratio between them is approximately 1.2, the attenuation coefficient for ^{201}Tl was estimated from that for ^{99m}Tc by multiplying it by 1.2 [9]. The data processor used was GMS-5500A/PI (Toshiba Medical Systems, Tochigi, Japan).

Fig. 2

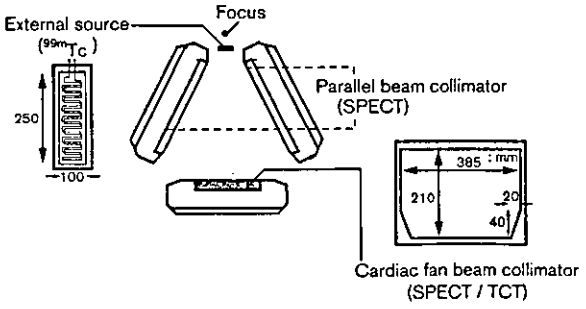

A 3-detector single photon emission computed tomography (SPECT) system used for simultaneous acquisition of transmission computed tomography (TCT)/SPECT data. The sheet shaped external gamma ray source for TCT was made from bellow tubes filled with 740 MBq of ^{99m}Tc was placed at the focus of the fan beam collimator.

The TCT and SPECT data were acquired simultaneously [10,11] using a matrix of 128 × 128 and step-and-shoot mode (30 s/projection angle) at an interval of 6° (60 projection angles for 360°). The pixel size was 3.2 mm. The counts in the TCT projection data were about 75 counts/pixel in the myocardial phantom and the myocardial area of patients, and were greater than 120 counts/pixel at the blank scan. Scatter correction was also performed using the triple-energy window (TEW) method [10]. The acquisition window width was set at 47% for the main window and 7% for the subwindow at 74 keV for ^{201}Tl, and 20% for the main window and 7% for the subwindow at 140 keV for ^{99m}Tc.

After truncation correction, the attenuation coefficient maps were generated from TCT data using the FBP method. When using the FBP method, a ramp convolution filter was used, and the high frequency noise in the reconstructed images was reduced using the Butterworth filter with a cut-off frequency of 0.44 cycle/cm and an order of 8. Subsequently, the projection data acquired using two detectors with parallel beam collimators were summed, and the SPECT images were reconstructed from these summed projection data using the ordered subsets expectation maximization (OSEM) method [12–14]. The number of subsets and of iterations were taken as 5 and 10, respectively.

Phantom study

Phantom studies were performed using a cylindrical phantom (200 mm in height and 200 mm in diameter) (AZ-660, Anzai-Sogyo, Tokyo, Japan) with or without hot rods. The hot rods (10, 15, 18 and 20 mm in diameter) were filled with ^{201}TlCl having a radioactivity of 92.5 kBq·ml^{-1}. When the hot rods were not used, the phantom was uniformly filled with ^{201}TlCl having a radioactivity of 9.25 kBq·ml^{-1}. The cylindrical phantom could be imaged inside the effective FOV (220 × 410 mm) of the fan beam collimator. The following three protocols were employed: protocol B with mild truncation of TCT data only, and protocol C with severe truncation of TCT data only. We compared the attenuation corrected SPECT images before and after truncation correction.

The phantom studies were also performed using a myocardial phantom (Data Spectrum Co., Hillsborough, NC, USA). This phantom could not be imaged inside the effective FOV of the fan beam collimator. A tracer (^{201}TlCl) with a radioactivity of 92.5 kBq·ml^{-1} was infused into the region of the myocardium and 9.25 kBq·ml^{-1} into the region of the chest as background.

The breasts were not taken into account in this study. The three protocols (A, B and C) given above were employed.

Human study

A normal 45-year-old man participated in this study. Informed consent was obtained after a detailed explanation of the purpose of the study and scanning procedures. Twenty minutes after intravenous injection of ^{201}TlCl (111 MBq), the TCT and SPECT data were acquired simultaneously. As in the myocardial phantom studies, the following three protocols given above were employed.

Results

Phantom study

Figure 3 summarizes the results of phantom studies using a cylindrical phantom. The first row illustrates the effective FOVs for TCT (solid circle) and SPECT (dashed circle). An illustration of the phantom with hot rods is also shown. The second row shows the TCT images. The third and fourth rows show the SPECT images of the phantom without and with hot rods, respectively. TC(−) and TC(+) represent the cases when the truncation was not corrected and corrected, respectively. As shown in Fig. 3(b) and (c), when the truncation was not corrected, artifacts due to truncation were observed. Figure 4 shows the profile curves through the line shown by an arrow on the SPECT image without hot rods in Fig. 3(a). In Fig. 4, the solid and dotted lines represent the cases when the truncation was corrected and not corrected, respectively. Even after truncation correction, there were approximately 4% and 22% errors in protocols B (Fig. 4(b)) and C (Fig. 4(c)), respectively, compared to the profile curve with truncation correction for protocol A (Fig. 4(a)). In protocol A, about a 5% error of maximum was observed before and after truncation correction. Figure 5 shows the profile curves through the line shown by an arrow in the SPECT image with hot rods (Fig. 3(a)). As in Fig. 4, the solid and dotted lines represent the cases when the truncation was corrected and not corrected, respectively. As shown in Fig. 5, good improvement was observed after truncation correction in all protocols, and the shape of the hot rods was also markedly improved especially in protocol C (Fig. 3(c)).

Figure 6 summarizes the results of using a myocardial phantom. As in Fig. 3, the first row illustrates the effective FOVs for TCT (solid circle) and SPECT (dashed circle), with the X-ray CT image of the phantom being superimposed. The second row shows the TCT images. The third and fourth rows show the transverse and short axis SPECT images of the phantom, respectively. As shown in Fig. 6, the truncation artifacts were observed on the TCT images in all

Fig. 3

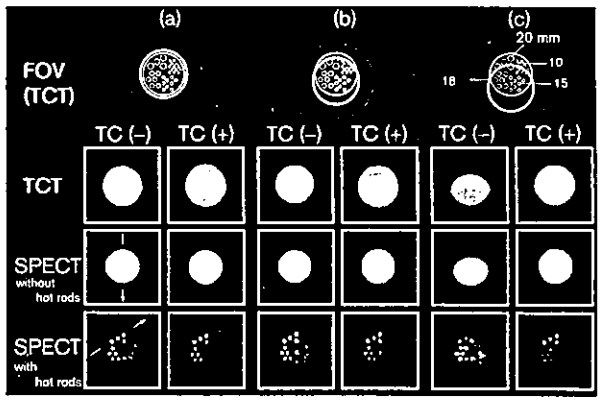

Results of phantom studies using a cylindrical phantom with or without hot rods. The first row illustrates the effective field of views (FOVs) for TCT (solid circle) and SPECT (dashed circle). An illustration of the phantom with hot rods is also shown. The second, third and fourth rows show the TCT images, and the SPECT images of the phantom without and with hot rods, respectively. Protocol A (panel a) includes no truncation of either TCT or SPECT data, protocol B (panel b) includes mild truncation of TCT data only, and protocol C (panel c) includes severe truncation of TCT data only. TC(−) and TC(+) represent the cases when the truncation was not corrected and corrected, respectively.

protocols. Figure 7 shows the profile curves through the line shown by an arrow on the short axis SPECT image for protocol A (Fig. 6(a)). When the truncation was not corrected, there were approximately 13% and 46% errors in protocols B (Fig. 7(b)) and C (Fig. 7(c)), respectively, as compared to the profile curve in the short axis SPECT image with truncation correction in protocol A (Fig. 7(a)). When the truncation was corrected, these errors rates decreased to less than 8%. In particular, marked improvement was observed in the area from the interventricular septum to the anterior wall in which truncation was observed on TCT and not on SPECT.

Human study

Figure 8 summarizes the results of human studies, and Fig. 9 shows the profile curves through the line shown by an arrow on the short axis SPECT image for protocol A (Fig. 8(a)). In protocol A, no marked error was observed on the short axis SPECT image (Fig. 8(a)) or the profile curve before and after truncation correction (Fig. 9(a)). In protocol B, good improvement of the TCT and SPECT images was observed (Fig. 8(b)), and the error (interventricular septum) in the profile curve was improved from 64% to 15% (Fig. 9(b)), compared to that obtained after truncation correction with protocol A (Fig. 9(a)). However, there was no improvement of the TCT and SPECT images after truncation correction in protocol C (Figs 8(c) and 9(c)).

Fig. 4

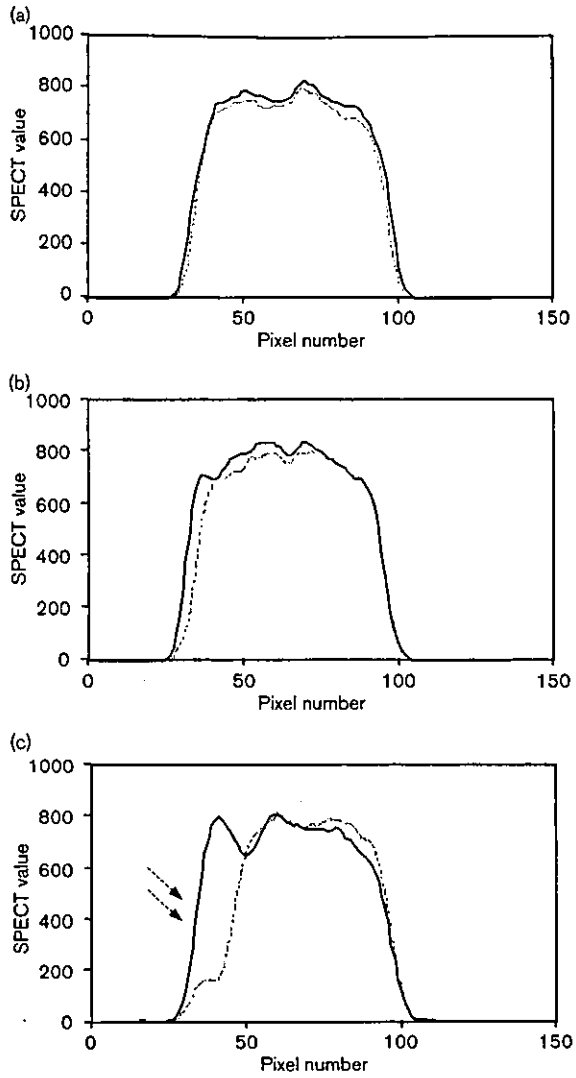

Profile curves through the line shown by an arrow on the SPECT image without hot rods in Fig. 3(a). The solid and dotted lines represent the cases when the truncation was corrected and not corrected, respectively. Panels a, b and c correspond to protocols A, B and C in Fig. 3, respectively.

Fig. 5

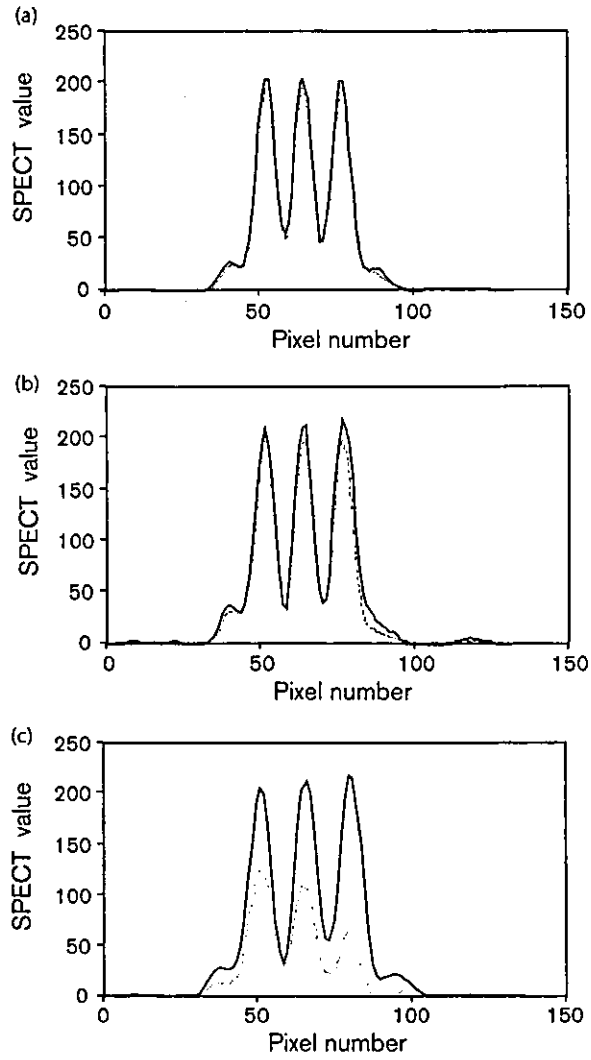

Profile curves through the line shown by an arrow on the SPECT image with hot rods in Fig. 3(a). The solid and dotted lines represent the cases when the truncation was corrected and not corrected, respectively. Panels a, b and c correspond to protocols A, B and C in Fig. 3, respectively.

Discussion

The simultaneous acquisition of TCT and SPECT data using 3-detector SPECT allows one to avoid additional TCT data acquisition for attenuation correction. The use of a fan beam collimator for TCT data acquisition is beneficial in that it reduces patient radiation dose and/or increases the pixel counts of the TCT data. However, a fan beam collimator may cause truncation on TCT due to the small effective FOV, eventually causing artifacts on SPECT images after attenuation correction. Although attenuation correction using TCT is not widely employed in the clinical setting, the reduction of truncation artifacts on TCT in simultaneous TCT/SPECT acquisition would enhance the application of attenuation correction using TCT. As previously described, the non-truncated projection data have two important properties [6,7]. Then, we speculated that the truncation artifacts on TCT might be corrected using the non-truncated SPECT data acquired with parallel beam collimators having a large FOV. Based on the above background, we

Fig. 6

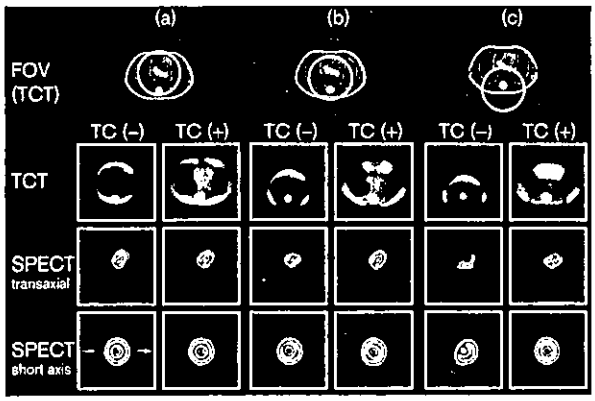

Results of phantom studies using a myocardial phantom. The first row illustrates the effective FOVs for TCT (solid circle) and SPECT (dashed circle), with the X-ray CT image of the phantom being superimposed. The second, third and fourth rows show the TCT, transaxial and short axis SPECT images of the phantom, respectively. Protocol A (panel a) includes no truncation of either TCT or SPECT data, protocol B (panel b) includes mild truncation of TCT data only, and protocol C (panel c) includes severe truncation of TCT and mild truncation of SPECT data. TC(–) and TC(+) represent the cases when the truncation was not corrected and corrected, respectively.

Fig. 7

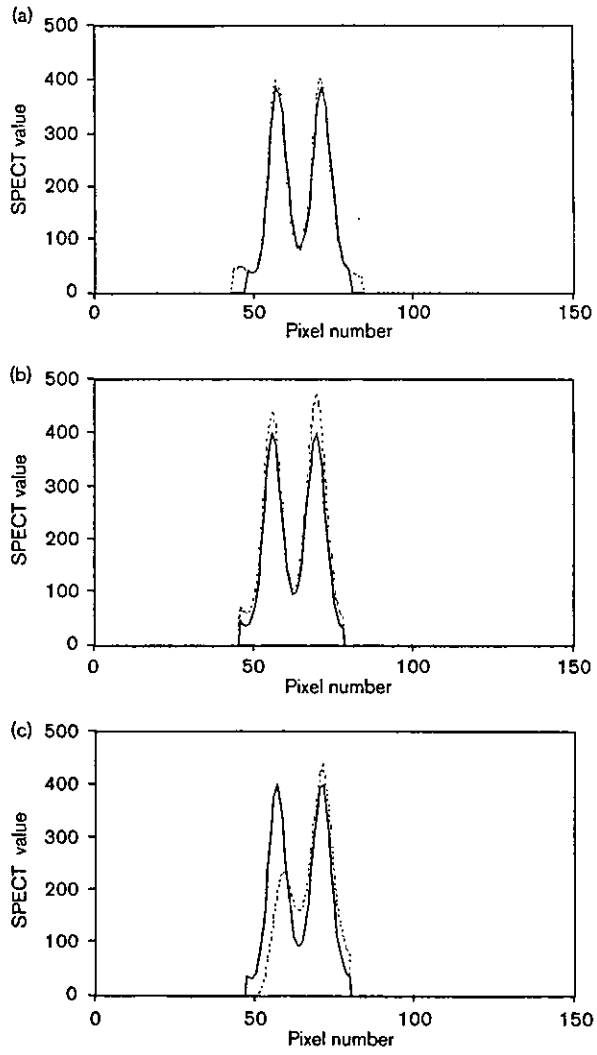

Profile curves through the line shown by an arrow on the short axis SPECT image in Fig. 6(a). The solid and dotted lines represent the cases when the truncation was corrected and not corrected, respectively. Panels a, b and c correspond to protocols A, B and C in Fig. 6, respectively.

developed a method of correcting for truncation artifacts on TCT, and our phantom and human studies (Figs 3–9) demonstrated that this method can adequately correct for the TCT truncation when the SPECT data are not truncated.

The attenuation correction using an external ^{99m}Tc gamma ray source in myocardial SPECT has been reported to improve the uniformity of the entire myocardium [15] and the specificity of diagnosis in the inferior wall region [16]. Our SPECT images corrected for attenuation using the truncation corrected TCT data were better and more uniform than those without attenuation correction. However, further clinical studies will be necessary to prove the advantage of attenuation corrected myocardial SPECT images over those without attenuation correction, because the incidence of over- or under-attenuation correction in each myocardial segment is unclear. The extent of improvement in the sensitivity, specificity and accuracy of diagnosis when the attenuation was corrected, should be demonstrated before its clinical use.

In 3-detector SPECT, an external gamma ray source can be placed at the opposite side of the fan beam collimator, that is, at its focus. This position appears to be effective for reducing the scattered gamma rays reaching the adjacent detectors [9,17].

It has been reported that when an attenuation coefficient map was generated using the FBP method, hot ring artifacts were present, while cold ring artifacts were obtained using the maximum likelihood expectation maximization algorithm [5]. Although we used the FBP method for TCT image reconstruction to reduce computation time in this study, we did not observe such ring artifacts. On the other hand, we used the OSEM method for SPECT image reconstruction [12]. Although we consider the FBP method better for TCT image

Fig. 8

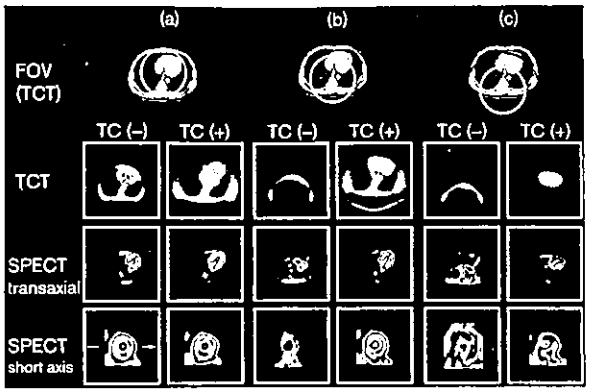

Results of human studies. The first row illustrates the effective FOVs for TCT (solid circle) and SPECT (dashed circle), with the X-ray CT image of the subject being superimposed. The second, third and fourth rows show the TCT, transaxial and short axis SPECT images, respectively. Protocol A (panel a) includes no truncation of TCT or SPECT data, protocol B (panel b) includes mild truncation of TCT data only, and protocol C (panel c) includes severe truncation of TCT and mild truncation of SPECT data. TC(−) and TC(+) represent the cases when the truncation was not corrected and corrected, respectively.

reconstruction and the OSEM method better for SPECT, a detailed investigation on the best combination of the methods for TCT and SPECT image reconstruction might be the subject of future studies.

In this study, ^{99m}Tc was used as an external gamma ray source because it was readily available. Evaluation of other external gamma ray sources such as ^{153}Gd [18,19] will be necessary in future studies.

In conclusion, we developed a method of correcting for truncation in TCT, and our phantom and human studies demonstrated that this method can adequately correct for the truncation of the TCT data acquired using a fan beam collimator in a 3-detector SPECT system, as long as there is no truncation of SPECT data. However, further studies will be necessary to establish the clinical usefulness of this method.

Acknowledgements

The authors thank Mr Kenzo Ide, Mr Shingo Izawa and Mr Kouichi Shiraishi (Nihon Medi-Physics Co., Ltd.) for their technical support.

References

1 Bailey DL, Hutton BF, Walker PJ. Improved SPECT using simultaneous emission and transmission tomography. *J Nucl Med* 1987; 28:844–851.
2 Murase K, Tanada S, Inoue T, Sugawara Y, Hamamoto K. Improvement of brain single photon emission tomography (SPET) using transmission data acqusition in a four-head SPET scanner. *Eur J Nucl Med* 1993; 20:32–38.
3 Jaszczak RJ, Gilland DR, Hanson MW, Jang S, Greer KL, Coleman RE. Fast transmission CT for determining attenuation maps using a collimated line source, rotatable air–copper–lead attenuators and fan-beam collimation. *J Nucl Med* 1993; 34:1577–1586.

Fig. 9

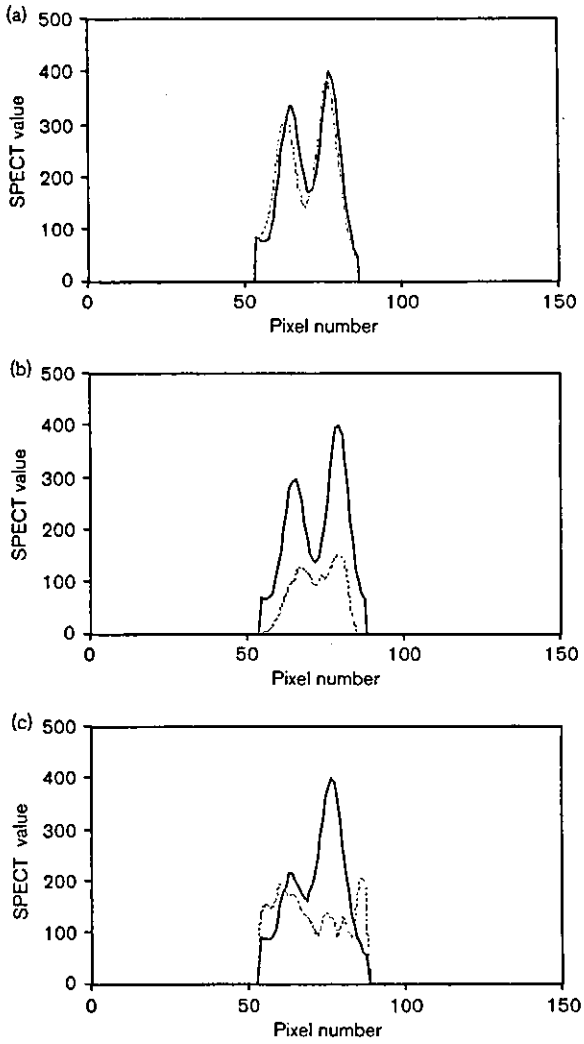

Profile curves through the line shown by an arrow on the short axis SPECT image in Fig. 8(a). The solid and dotted lines represent the cases when the truncation was corrected and not corrected, respectively. Panels a, b and c correspond to protocols A, B and C in Fig. 8, respectively.

4 Pan T-S, King MA, Penney BC, Rajeevan N, Luo D-S, Case JA. Reduction of truncation artifacts in fan beam transmission by using parallel beam emission data. *IEEE Trans Nucl Sci* 1995; 42:1310–1320.
5 George KG, Benjamin MW, Grant TG. Effect of truncated projections on defect detection in attenuation-compensated fan beam cardiac SPECT. *J Nucl Med* 1998; 39:166–175.
6 Kadrmas DJ, Jaszczak RJ, McCormick JW, Coleman RE, Lim CB. Truncation artifact reduction in transmission CT for improved SPECT attenuation compensation. *Phys Med Biol* 1995; 40:1085–1104.
7 Motomura N, Ichihara T, Takayama T, Nishihara K, Inouye T, Kataoka T, *et al.* Practical method for reducing truncation artifacts in a fan beam transmission CT system [Abstract]. *J Nucl Med* 1998; 25:178p.
8 Hosoba M, Wani H, Toyama H, Murata H, Tanaka E. Automated body contour detection in SPECT: effects on quantitative studies. *J Nucl Med* 1986; 27:1184–1191.

9 Tsui BMW, Gullberg GT, Edgerton ER. Correction of nonuniform attenuation in cardiac SPECT imaging. *J Nucl Med* 1989; 30:497–507.

10 Ichihara T, Motomura N, Ogawa K, Hasegawa H, Hashimoto J, Kubo A. Evaluation of SPET quantification of simultaneous emission and transmission imaging of the brain using a multidetector SPET system with the TEW scatter compensation method and fan-beam collimation. *Eur J Nucl Med* 1996; 23:1292–1299.

11 Vidal R, Buvat I, Darcourt J, Migneco O, Desvignes P. Impact of attenuation correction by simultaneous emission/transmission tomography on visual assessment of ^{201}Tl myocardial perfusion images. *J Nucl Med* 1999; 40:1301–1309.

12 Hudson HM, Larkin RS. Accelerated image reconstruction using ordered subsets of projection data. *IEEE Trans Med Imaging* 1994; MI-13: 601–609.

13 Murase K, Tanada S, Sugawara Y, Tauxe WN, Hamamoto K. An evaluation of the accelerated expectation maximization algorithms for single-photon emission tomography image reconstruction. *Eur J Nucl Med* 1994; 21:597–603.

14 Takahashi Y, Murase K, Higashino H, Sogabe I, Sakamoto K. Receiver operating characteristic (ROC) analysis of image reconstructed with iterative expectation maximization algorithms. *Ann Nucl Med* 2001; 15: 521–525.

15 Hashimoto J, Ogawa K, Kubo A, Ichihara T, Motomura N, Takayama T. Application of transmission scan-based attenuation compensation to scatter-corrected thallium-201 myocardial single-photon emission tomographic images. *Eur J Nucl Med* 1998; 25:120–127.

16 Rosenthal MS, Cullom J, Hawkins W, Moore SC, Tsui BMW, Yester M. Quantitative SPECT imaging: a review and recommendations by the Focus Committee of the Society of Nuclear Medicine Computer and Instrumentation Council. *J Nucl Med* 1995; 36:1489–1513.

17 Frey EC, Tsui BMW, Perry JR. Simultaneous acquisition of emission and transmission data for improved thallium-201 cardiac SPECT imaging using a technetium-99 m transmission source. *J Nucl Med* 1989; 33: 2238–2245.

18 He Z-H, Scarlett MD, Mahmarian JJ, Verani MS. Enhanced accuracy of defect detection by myocardial single-photon emission computed tomography with attenuation correction with gadolinium-153 line sources: evaluation with a cardiac phantom. *J Nucl Cardiol* 1997; 4: 202–210.

19 VanLaere K, Koole M, Kauppinen T, Monsieurs M, Bouwens L, Dierck R. Nonuniform transmission in brain SPECT using ^{201}Tl, ^{153}Gd, and ^{99m}Tc static line sources: anthropomorphic dosimetry studies and influence on brain quantification. *J Nucl Med* 2000; 41:2051–2062.

ORIGINAL ARTICLE

Annals of Nuclear Medicine Vol. 18, No. 7, 585–590, 2004

A study on attenuation correction using Tc-99m external TCT source in Tc-99m GSA liver SPECT

Yasuyuki TAKAHASHI,* Kenya MURASE,* Teruhito MOCHIZUKI,** Hiroshi HIGASHINO,***
Yoshifumi SUGAWARA** and Akiyoshi KINDA****

*Department of Medical Engineering, Division of Allied Health Sciences, Osaka University Graduate School of Medicine
**Department of Radiology, Ehime University School of Medicine
***Department of Radiology, Ehime Prefectural Imabari Hospital
****Toshiba Medical Engineering Laboratory

Purpose: In attenuation correction of ECT images by transmission CT (TCT) with an external ^{99m}Tc γ-ray source, simultaneous TCT/ECT data acquisition is difficult, when the same radionuclide such as ^{99m}Tc-tetrofosmin or ^{99m}Tc-GSA is used as the tracer. In this case, TCT is usually acquired before administration of the tracer, and ECT is acquired separately after the tracer injection. However, mis-registration may occur between the TCT and ECT images, and the repetition of examinations add to the mental and physical stress of the patients. In this study, to eliminate this problem, we evaluated whether attenuation correction of ECT images can be achieved by acquiring TCT and ECT simultaneously, then acquiring ECT alone, and preparing an attenuation map by subtracting the latter from the former using ^{99m}Tc-GSA liver ECT. ***Method:*** The ECT system used was a three-head gamma camera equipped with one cardiac fan beam collimator and two parallel beam collimators. External γ-ray source for TCT of ^{99m}Tc was 740 MBq, and ECT of ^{99m}Tc-GSA was 185 MBq. First, pure TCT data were acquired for the original TCT-map, then, ECT/TCT data were acquired for the subtracted TCT-map, and finally, pure ECT data were acquired. The subtracted attenuation map was produced by subtracting the pure ECT image from the TCT/ECT image, and attenuation correction of the ECT image was done using both this subtracted TCT map and attenuation map from pure TCT. These two attenuation corrected images and non-corrected images were compared. Hot rods phantom, a liver phantom with a defect, and 10 patients were evaluated. ***Results:*** Attenuation corrected ECT values using the subtraction attenuation map showed an error of about 5% underestimation compared with ECT values of the images corrected by original attenuation map at the defect in the liver phantom. A good correlation of $y = 22.65 + 1.06x$, $r = 0.958$ was observed also in clinical evaluation. ***Conclusion:*** By means of the method proposed in this study, it is possible to perform simultaneous TCT/ECT data acquisition for attenuation correction using Tc-99m external source in Tc-99m GSA liver SPECT. Moreover, it is thought that this method decreases the mental and physical stress of the patients.

Key words: transmission computed tomography, ^{99m}Tc-GSA, subtraction attenuation map

INTRODUCTION

RECENTLY, ^{99m}Tc preparations, which are convenient for emergency examinations, are commonly used as tracers for nuclear medicine examinations, e.g. ^{99m}Tc-HM-PAO for imaging of the cerebral blood flow and ^{99m}Tc-tetrofosmin for imaging of myocardial perfusion. For transmission computed tomography (TCT), ^{99m}Tc is also used as a relatively available external source.[1,2] However,

Received April 1, 2003, revision accepted June 27, 2004.

For reprint contact: Yasuyuki Takahashi, Ph.D., Department of Health, Health Planning Division, Ehime Prefectural Matsuyama Regional Office, 132, Kita-mochida, Matsuyama, Ehime 790–8502, JAPAN.

E-mail: takahashi-yasuyuki@pref.ehime.jp

if the same nuclide is used, TCT and ECT must be acquired separately. But the effects of the registration errors between TCT and ECT images, and the repetition of examinations increases the mental and physical stress of the patients.

TCT/ECT simultaneous acquisition can be performed by SPECT/CT system, or TCT (Gd-153)/ECT (Tc-99m) dual-isotope SPECT; however, the radioactive half life of ^{153}Gd of external source in these systems is as short as 240 days, and these isotopes are expensive. Therefore, if Tc-99m is used as an external source, attenuation correction could be performed easily at a low cost, although there is a problem with the present regulation system. To avoid mis-registration, it is necessary to perform TCT and ECT in the simultaneous mode.[3]

In this study, we, therefore, evaluated the feasibility of the method in which TCT and ECT are acquired simultaneously, then ECT alone is performed, using the same Tc-99m as the radiopharmaceuticals for imaging and a TCT map, which was generated by subtracting the latter from the former. ECT is corrected using this map. In this study, the effect of attenuation correction by this method was evaluated by comparing images a TCT alone to obtain an original attenuation map before the injection of the tracer for simultaneous TCT and ECT and comparing the results of correction using this original attenuation non-corrected and corrected by the subtraction TCT map and by the original TCT map.

MATERIALS AND METHODS

ECT system and condition

The ECT system used was a GCA-9300A/UI (Toshiba Medical Systems, Tochigi, Japan) equipped with one cardiac fan beam collimator and two parallel beam collimators, with the data processor also Toshiba, GMS-5500A/PI. The TCT external γ-ray source was a sheet-shape made from a bellows tube filled with 740 MBq of ^{99m}Tc. The tube was 1 mm in the inner diameter made of fluorocarbon resin embedded in an acrylic rectangular board of 250 × 100 mm.

Both TCT and ECT images were sampled with a matrix size of 128 × 128, continuous mode (15 min/rotation) at intervals of 6 degrees (60 directions, 360-degree acquisition/detector). The pixel size was 3.2 mm. With these parameters, the count per detector in the phantom study was about 75 counts/pixel; and the counts/pixel in the myocardial area of patients was higher than 120. According to the triple-energy window (TEW) method,[4] the acquisition window widths were 20% for the main window at 140 keV of ^{99m}Tc and 7% for the lower subwindow.

After truncation correction, attenuation maps of TCT acquisition data[5] were produced by the filtered back projection (FBP) method. Subsequently, parallel beam projection data of the 2 detectors for ECT imaging were summated, then TEW scatter correction (SC) was performed and ECT images were reconstructed using Ordered Subsets-Expectation Maximization (OS-EM).[6–8]

The ECT acquisition data were reconstructed with a ramp convolution filter, and high frequency noise was decreased with post-reconstruction Butterworth filtering (cutoff frequency = 0.44 cycle/cm).

Data acquisition and imaging protocols

In the phantom study, ^{99m}Tc was filled in the phantom, then, protocol A′ (TCT + ECT) was acquired with the external source, followed by protocol A″ (ECT only) which was acquired without the external source. Then, a subtraction attenuation map (S-Map) was generated by subtracting data (protocol A′ – protocol A″), and attenuation corrected ECT images of the protocol A″ were reconstructed. In the phantom study, the phantom was left as it was for four days, a TCT source was placed again after 96 hours, then protocol A (TCT only) was acquired. An original attenuation map (O-Map) was generated by protocol A alone.

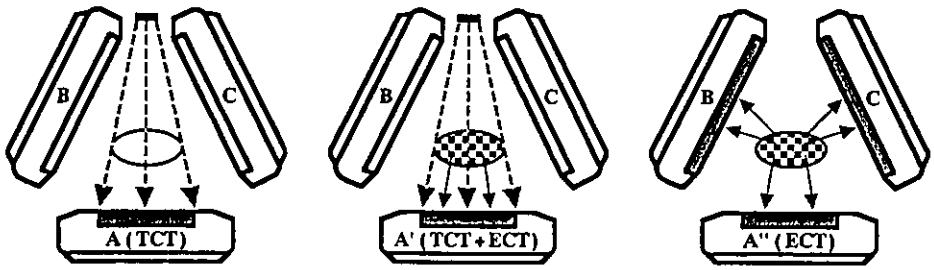

A,B,C : detector
A : fan-beam collimator (transmission scan, external source),
A' : fan-beam collimator (transmission scan, external source and emission scan),
A" : fan-beam collimator (transmission scan, non-external source and emision scan),
B, C : parallel beam collimator (emission scan)
A'-A" : subtraction transmission scan

Fig. 1 The all directions method of data acquisition is shown.
(a) original TCT, (b) TCT and ECT simultaneous acquisition, (c) ECT

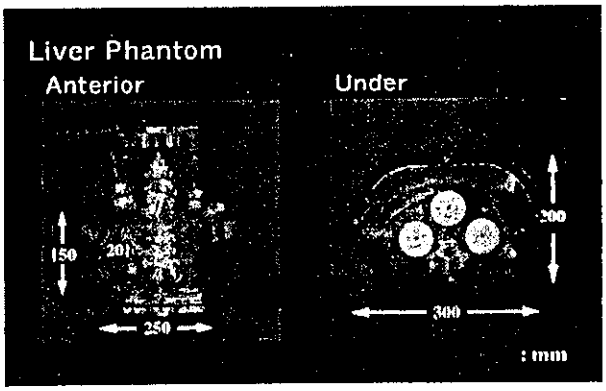

Fig. 2 The appearance of the liver phantom.

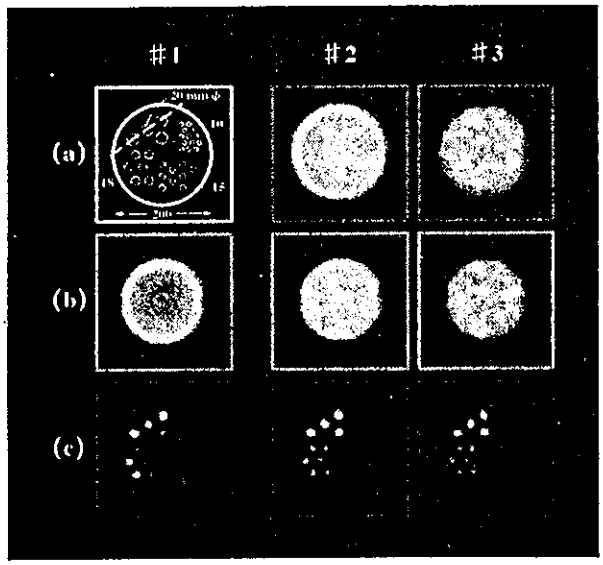

Fig. 3 (a) A scheme and an attenuation map of the columnar phantom, (b) a SPECT image of a uniformity phantom, and (c) a SPECT image of a hot rods phantom. #1: No attenuation correction. #2: Original TCT. #3: Subtraction TCT.

In the human study, protocol A was acquired first, then protocol A′ was acquired, and finally protocol A″ was acquired. Attenuation corrected ECT images of the protocol A″ reconstructed using O-Map and S-Map were compared (Fig. 1). The acquisition time was 15 minutes in all cases.

Phantom study

In the cylindrical phantom (200 mm × 200 mm × 200 mm circle, AZ-660, Anzai-Sogyo, Tokyo, Japan), areas filled with uniform tracer activity (92.5 kBq/m*l*) and hot rods areas (9.25 kBq/m*l*) were created, and the image quality was compared using uniformity and hot rods (#1 (a) in Fig. 3). The ECT images after attenuation correction using the S-Map and O-Map were compared with the uniformity phantom with the profile curves and normalized root mean square errors (NRMSE (%), $\sqrt{[\Sigma(X_i - O_i)^2 / \Sigma O_i^2]} \times 100$; X_i, subtraction image; O_i, original image; i, pixel number ($i = 1 - n$)). Spatial resolution of the hot rods phantom was evaluated with the profile curves.

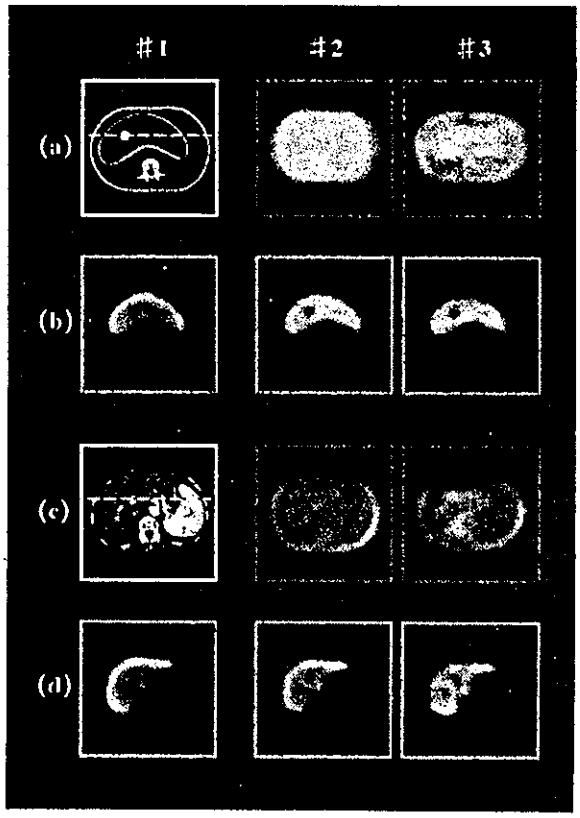

Fig. 4 (a) Schemes and attenuation maps of the liver phantom and a clinical case, (b) phantom SPECT images. (c) abdomen (liver) CT images and (d) abdomen (liver) ECT images. #1: No attenuation correction. #2: Original TCT. #3: Subtraction TCT.

In the liver phantom (LSF-type, Kyoto-Kagaku, Kyoto, Japan, Fig. 2), the concentration of ^{99m}Tc in the liver part was 247 kBq/m*l* [9] and the body part was 24.7 kBq/m*l*. In this study, a spherical defect of 20 × 20 mm in diameter was established in the left lobe, and ECT images after attenuation correction using S-Map and O-Map were compared with regard to the clarity of the defect image using profile curves.

Human study

As a human study, a 60-year-old female patient with liver cirrhosis diagnosed on the basis of clinical and CT findings was evaluated. The acquisition times of ECT and TCT were the same. Before administration of ^{99m}Tc-GSA, transmission data (protocol A) were acquired first. Then, 15 minutes after the intravenous injection of 185 MBq of ^{99m}Tc-GSA, simultaneous TCT/ECT data (protocol A′) were acquired with an external source (740 MBq of ^{99m}Tc). Finally, only ECT data (protocol A″) of ^{99m}Tc-GSA were acquired without an external source (Fig. 1).

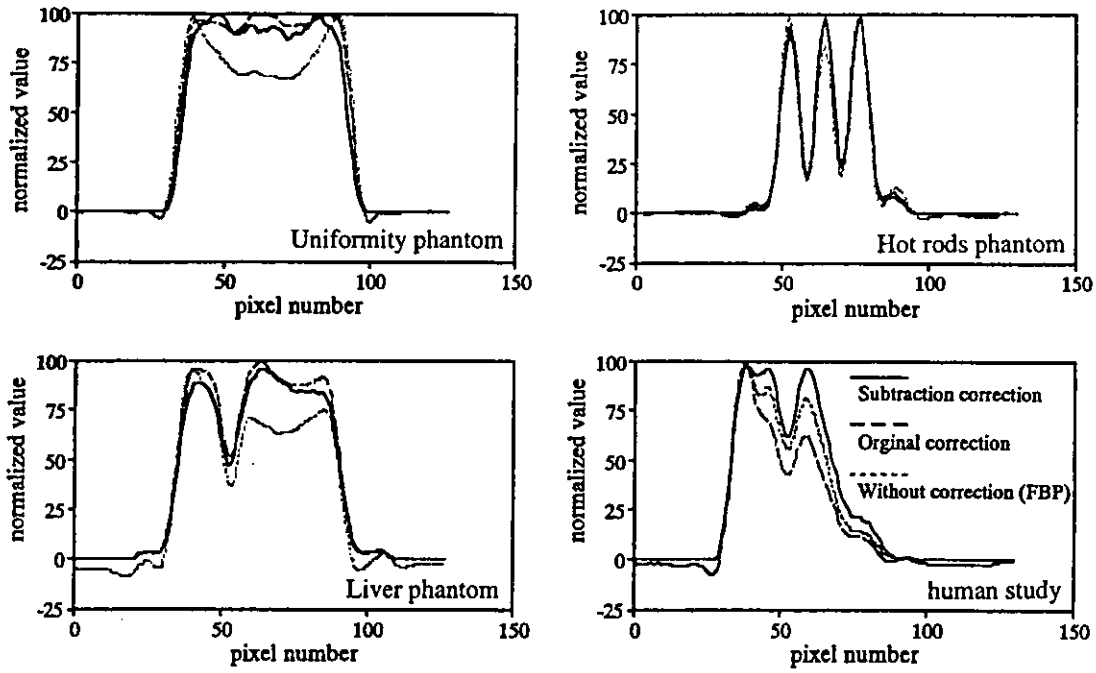

Fig. 5 CPR at the dotted line in each scheme. *Upper left*, uniformity phantom; *upper right*, hot rods phantom; *lower left*, liver phantom; *lower right*, case study.

S-Map was prepared by the subtraction, and O-Map was prepared from protocol A. In protocol A and protocol A″, 4 markers were placed on the body surface as the landmarks for the Automatic Registration Tool (ART),[10] and ECT images after attenuation correction using S-Map and O-Map were compared.

Human materials consisted of 10 patients (7 liver cirrhosis [4 males and 3 females aged 65 ± 6 years], and 3 hepatocellular carcinoma [2 males and 1 females aged 67 ± 5 years]).

RESULTS

Phantom study

The transaxial images of the uniformity phantom are shown in Figure 3 (b), and the place for the count profile curves (Table 1, *upper left*) shown as the broken line #1 (a) in Figure 3. The ECT values (mean ± SD, [CV(%)]) are for the internal side at both ends of the transaxial image: O-map 92.33 ± 3.52 [3.81], S-map 95.96 ± 1.94 [2.02], and ECT values without attenuation correction were 78.54 ± 15.60 [19.86]. ECT values using the S-Map was overestimated by about 9% near the center. The NRMSE in these images were 10.5%.

Figure 3 (c) shows the transaxial images of the hot rods phantom. The profile curves (Fig. 5, *upper right*) were nearly identical. Visualization was similar.

Defect in the liver phantom was shown as dotted lines in the scheme. Normalized ECT values of the defects (minimum value) using the S-Map were 10% better than those using the O-Map (Fig. 5, *lower left*). Over correction of 4–7% was observed in the center and peripheries (Fig. 5, *upper right*).

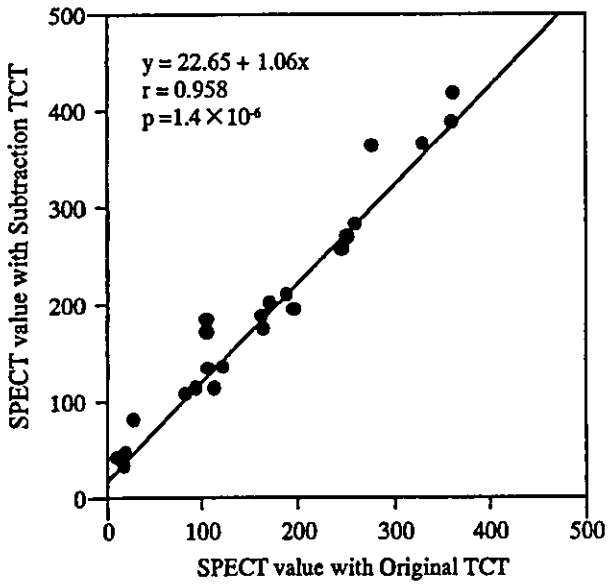

Fig. 6 Comparison of ECT values in 25 ROI including SOL and hepatectomy sites in 10 patients.

Human study

The case (Fig. 4) presented here had liver cirrhosis with mild swelling of the left lobe. After angiography, a defect

of GSA was noted at the porta hepatis. The normalized ECT value of the defect (CPR in the area surrounded by the dotted line in the scheme; Fig. 5, *lower right*) was reduced by 10% with the S-Map as compared with the O-Map. In the caudate lobe, a 12% overestimation was observed.

In the 25 ROIs in 10 patients, the ECT values after attenuation correction using the O-Map and S-Map showed a good correlation ($y = 22.65 + 1.06x$, $r = 0.958$, $p = 1.4 \times 10^{-6}$).

DISCUSSION

For attenuation correction of ECT images by TCT with an external source, TCT with ^{153}Gd can be acquired in combination with ECT simultaneously using tracers such as ^{201}Tl and ^{99m}Tc-MIBI in myocardial scintigraphy.[11] In an evaluation using TCT in the liver,[12] good quantitative results of volume measurements were reported.[13] In a liver ^{99m}Tc-GSA scintigraphy which is an analog ligand of the asialoglycoprotein receptor, it is report and attenuation correction is necessary in the quantitative evaluation of the liver.[14]

^{99m}Tc can also be used as an external source for TCT; however, TCT/ECT simultaneous acquisition[2] can not be used, when the same ^{99m}Tc radiotracer such as ^{99m}Tc-GSA is used. In the sequential mode,[14] TCT must be acquired before the administration of the tracer, and ECT thereafter can be acquired. However a mis-registration may between when TCT and ECT images for attenuation correction.[15] The mis-registration must be avoided by use of the ART method.[11] In sequential mode, improvement of concentration linearity was reported by combination of TCT attenuation correction and TEW scatter compensation.[14] Since the external source is comparatively large, TEW scatter compensation can also correct ECT scatter as well as TCT scatter.[16]

In order to reduce the repetition of examinations, we examined whether attenuation correction can be performed by acquiring TCT and ECT twice serially in the simultaneous mode and acquiring an attenuation map by image subtraction. When the protocol "simultaneous TCT/ECT (^{99m}Tc-GSA) followed ECT", i.e., (1) i.v. of radiotracer, (2) waiting for fixation of the radiotracer, (3) TCT/ECT, (4) ECT, subtracted TCT map (TCT/ECT – ECT) can be generated. This protocol saves the time needed for fixation of the radiotracer, compared with the conventional protocol "TCT (GSA) followed ECT", i.e., (1) TCT, (2) i.v. of radiotracer, (3) waiting for fixation, (4) ECT. In the phantom study, to minimize mis-registration between the ECT and TCT images, TCT and ECT were acquired simultaneously, ECT alone was then acquired, and original TCT was acquired after the phantom was allowed to stand for 96 hours in consideration of the attenuation time. However, as this protocol is difficult in clinical cases, markers were placed at 4 points on the phantom, and images were overlayed by the landmark method of the ART.[10] In the experiments using uniformity, hot rods and liver phantoms, no marked difference was observed between the O-map and S-map, and a 5% error was observed in the defect value in the liver phantom with a model SOL. In human study, also, errors of ECT values in the defects after hepatectomy and relatively large SOL (space occupying lesion) of 3 cm or greater in diameter were 0–7%, but they were larger and more variable with a maximum of 20% for small tumors about 1 cm in diameter or other hepatic resions. Since this value was within the limits of agreement (mean ± 2SD) of the evaluation method of Bland & Altman,[17] it is clinically acceptable. However, there was no such error in the phantom study, and therefore, a part of the errors may due to respiration, which is uncorrectable by the subtraction method. Evaluation of the respiratory affect and its correction must be performed using respiratory gated[18] liver SPECT in future studies.

The subtraction method in ^{99m}Tc-GSA must take pharmacokinetic analyses into consideration; namely the liver is described in 30 seconds after injection, the tracer is accumulated rapidly, and after 15 to 40 minutes has comparatively little change in time-activity.[19] Therefore, TCT and ECT were acquired at the same time. Moreover, time-activity is considered to decrease more by acquiring continuous repetitive rotation of the gamma camera.[20] Since about 50% of the amount of administered ^{99m}Tc-GSA is accumulated in the liver,[19] sufficient radiotracer counts are obtained in the liver ECT may be obtained using one detector with parallel beam collimator. Then two other detectors may be used for TCT with high radioactivity counts. This method may improve the accuracy of TCT attenuation correction.

CONCLUSION

By means of the subtraction attenuation correction method proposed in this study, it is possible to perform simultaneous TCT/ECT data acquisition for attenuation correction using Tc-99m external source in Tc-99m GSA liver SPECT. Moreover, it is thought that this method decreases the mental and physical surden of the patients.

REFERENCES

1. Murase K, Tanada S, Inoue T, Sugawara Y, Hamamoto K. Improvement of brain single photon emission tomography (SPET) using transmission data acquisition in a four-head SPET scanner. *Eur J Nucl Med* 1993; 20: 32–38.
2. Jaszczak RJ, Gilland DR, Hanson MW, Jang S, Greer KL, Coleman RE. Fast Transmission CT for Determining Attenuation Maps Using a Collimated Line Source, Rotatable Air-Copper-Lead Attenuators and Fan-Beam Collimation. *J Nucl Med* 1993; 34: 1577–1586.
3. Ficaro EP, Fessler JA, Ackermann RJ, Rogers WL, Corbett JR, Chwaiger M. Simultaneous transmission-emission

thallium-201 cardiac SPECT: effects of attenuation correction on myocardial tracer distribution. *J Nucl Med* 1995; 36: 921–931.
4. Ogawa K. Simulation study of triple-energy-window scatter correction in combined Tl-201, Tc-99m SPECT. *Ann Nucl Med* 1995; 8: 277–281.
5. Motomura N, Ichihara T, Takayama T, Nishihara K, Inouye T, Kataoka T, et al. Practical method for reducing truncation artifacts in a fan beam transmission CT system. *J Nucl Med* 1998; 39: (Suppl) 178.
6. Hudson HM, Larkin RS. Accelerated image reconstruction using ordered subsets of projection data. *IEEE Trans Med Imaging* 1994; MI-13: 601–609.
7. Murase K, Tanada S, Sugawara Y, Tauxe WN, Hamamoto K. An evaluation of the accelerated expectation maximization algorithms for single-photon emission tomography image reconstruction. *Eur J Nucl Med* 1994; 21: 597–603.
8. Takahashi Y, Murase K, Higashino H, Sogabe I, Sakamoto K. Receiver operating characteristic (ROC) analysis of image reconstructed with iterative expectation maximization algorithms. *Ann Nucl Med* 2001; 15: 521–525.
9. Torizuka K, Ha-Kawa SK, Ikekubo K, Suga Y, Tanaka Y, Hino M, et al. Phase I clinical study on ^{99m}Tc-GSA, a new agent for functional imaging of the liver. *KAKU IGAKU (Jpn J Nucl Med)* 1991; 28: 1321–1331. (in Japanese)
10. Ardekani BA, Braun M, Hutton BF, Kanno I, Iida H. A Fully Automatic Multimodality Image Registration Algorithm. *J Comput Assist Tomogr* 1995; 19: 615–623.
11. Laere DL, Koole M, Kauppinen T, Monsieurs M, Bouwens L, Dierck R. Nonuniform Transmission in Brain SPECT Using ^{201}Tl, ^{153}Gd, and ^{99m}Tc Static Line Sources: Anthropomorphic Dosimetry Studies and Influence on Brain Quantification. *J Nucl Med* 2000; 41: 2051–2062.
12. Malko JA, Van Heertum RL, Gullberg GT, Kowalsky WP. SPECT liver imaging using an iterative attenuation correction algorithm and external flood source. *J Nucl Med* 1986; 27: 701–705.
13. Strauss LG, Clorius JH, Frank T, Van Kaick G. Single photon emission computerized tomography (SPECT) for estimates of liver and spleen volume. *J Nucl Med* 1984; 25: 81–85.
14. Ichihara T, Maeda H, Yamakado K, Motomura N, Matsumura K, Takeda K, et al. Quantitative analysis of scatter- and attenuation-compensated dynamic single-photon emission tomography for functional hepatic imaging with a receptor-binding radiopharmaceutical. *Eur J Nucl Med* 1997; 24: 59–67.
15. Murase K, Tanada S, Inoue T, Sugawara Y, Hamamoto K. Effect of misalignment between transmission and emission scans on SPECT images. *J Nucl Med Technol* 1993; 21: 152–156.
16. Matsumoto M, Kojima A, Ooyama Y, Kira T, Kira M, Yokoyama T, et al. An investigation of the scatter from TCT data using sheet source and its compensation. *KAKU IGAKU (Jpn J Nucl Med)* 1997; 34: 701. (in Japanese)
17. Bland JM, Altman DG. Statistical methods for assessing agreement between two methods of clinical measurement. *Lancet* 1986; 1: 307–310.
18. Cho K, Kumita S, Okada S, Kumazaki T. Development of respiratory gated myocardial SPECT system. *J Nucl Cardiol* 1999; 6: 20–28.
19. Ha-kawa SK, Nakanishi K, Kojima M, Tanaka Y, Kitagawa S, Kubota Y, et al. Clinical application of asialoglycoprotein receptor-mediated liver scintigraphy using ^{99m}Tc-DTPA-galactosyl-human serum albumin. *Jpn J Radiol Soc* 1991; 51: 1489–1497. (in Japanese)
20. Takahashi Y, Matsuki H, Mochizuki T. Basic study of continuous repetitive data acquisition using a phantom. *KAKU IGAKU (Jpn J Nucl Med)* 1996; 33: 1363–1369. (in Japanese)

Int J Clin Oncol (2004) 9:503–509
DOI 10.1007/s10147-004-0440-2

ORIGINAL ARTICLE

Syuichi Shinohara · Takashi Ochi · Tatsuhiko Miyazaki
Takashi Fujii · Masashi Kawamura · Teruhito Mochizuki
Masaharu Ito

Histopathological prognostic factors in patients with cervical cancer treated with radical hysterectomy and postoperative radiotherapy

Received: December 24, 2003 / Accepted: August 2, 2004

Abstract
Background. Many studies have been performed, on the clinical outcome and prognostic factors in patients with cervical cancer treated with radical hysterectomy and postoperative radiotherapy, but no useful method for predicting the risk of recurrence has been established. The purpose of this study was to analyze histopathological prognostic factors. In addition, we proposed a new risk classification and evaluated its usefulness.
Methods. One hundred and thirty patients with stage I-II uterine cervical cancer were treated with radical hysterectomy and postoperative radiotherapy at Ehime University Hospital between 1978 and 1997. All surgical specimens were reviewed, and the relationship between histopathological factors and the clinical outcome was analyzed.
Results. Of the histopathological prognostic factors of the surgical specimens analyzed, six factors (parametrial invasion, venous infiltration, pelvic lymph node metastases, thickness of the residual muscular layer, tumor depth, and tumor growth pattern) were significant prognostic factors. In particular, venous infiltration and pelvic lymph node metastases were strongly correlated with recurrence. Using the above five factors (excluding the thickness of the residual muscle layer), all patients were scored based on the total number of poor prognostic factors, and were classified into three groups. Patients with a score of 0–1 were classified as the low-risk group, those with a score of 2 as the intermediate group, and those with a score of 3–5 as the high-risk group. The 5-year disease-free survival rates were 93% in the low-risk group, 82% in the intermediate group, and 56% in the high-risk group ($P < 0.05$).
Conclusion. Six prognostic factors were found. Our risk classification seems to be clinically useful to predict which patients are at risk of recurrence.

Key words Uterine cervical cancer · Postoperative radiotherapy · Prognostic factor

S. Shinohara (✉) · T. Ochi · T. Fujii · T. Mochizuki
Department of Radiology, Ehime University School of Medicine, Shitsukawa, Shigenobu-cho, Ehime 791-0295, Japan
Tel. +81-89-960-5371; Fax +81-89-960-5375
e-mail: sshinoha@m.ehime-u.ac.jp

T. Miyazaki
Second Department of Pathology, Ehime University School of Medicine, Ehime, Japan

M. Kawamura
Department of Radiology, Nara Social Insurance Hospital, Nara, Japan

M. Ito
Department of Obstetrics and Gynecology, Ehime University School of Medicine, Ehime, Japan

Introduction

Radical hysterectomy or radical radiotherapy is the primary therapy for early-stage uterine cervical cancer. Similar clinical outcomes have been reported with these two strategies.[1] Many patients have been treated with surgery in Japan, and there are many studies about the prognostic factors of early-stage cervical cancer treated with surgery. The prognosis is poor in patients with either lymph node metastases, parametrial invasion, bulky tumor, deep stromal invasion, vascular infiltration, or a positive vaginal stump.[2,3] In these patients, postoperative radiotherapy is usually employed as additional therapy. The effect of postoperative radiotherapy on improving local control has been demonstrated; however, its role in increasing survival is controversial.[3–5] The recurrence rate in patients treated with radical hysterectomy and postoperative radiotherapy has been reported to be 15%–40%.[4–9] Many studies have been performed about the prognostic factors, and several histopathological prognostic factors have been reported.[3–23] Nevertheless, no useful method has been established for predicting which patients are at risk of recurrence. Therefore, the purpose of this study was to analyze the histopathological prognostic factors related to recurrence in patients treated with radical hysterectomy and postoperative radiotherapy and to propose a useful method for predicting the risk of recurrence.

Patients and methods

Patients

Between January 1978 and December 1997, 130 patients with uterine cervical cancer were treated with radical hysterectomy and postoperative radiotherapy at Ehime University Hospital. The patients' ages ranged from 28 to 72 years, and the median age was 49 years.

The clinical stage, judged according to the International Federation of Gynecology and Obstetrics (FIGO) stages, was stage IB in 88 patients, stage IIA in 15, and stage IIB in 27. The histological types of tumor were non-keratinizing squamous cell carcinoma in 82 patients, keratinizing squamous cell carcinoma in 34, and adenocarcinoma in 14.

Postoperative radiotherapy

Indications for postoperative radiotherapy were assessed according to the *General rules for clinical and pathological management of uterine cervical cancer*[2]: (a) lymph node metastases, (b) parametrial invasion, (c) marked primary invasion or vascular infiltration, and (d) insufficient vaginal wall excision. For the postoperative radiotherapy, external irradiation was performed using a linear accelerator, and anteroposterior opposing portal irradiation of 10-MV X-ray was administered. The upper and lower margins of the irradiation field were the top of L5 and the lower margin of the obturator foramen. The left and right margins were 1.5–2 cm lateral to the widest diameter of the pelvic outlet. A total dose of 40–60 Gy (median, 50 Gy) was given, with 1.8 Gy or 2.0 Gy per fraction.

Histopathological findings

All surgical specimens were reviewed histopathologically, and evaluated according to *the general rules for clinical and pathological management of uterine cervical cancer*.[2] Histopathological factors investigated were as follows: (1) histological type of tumor, (2) pathological T factor (pT), (3) corpus invasion, (4) vaginal invasion, (5) lymph vessel infiltration, (6) venous infiltration, (7) pelvic lymph node metastases, (8) tumor growth pattern, (9) tumor width, (10) tumor depth, and (11) thickness of the residual normal muscular layer. We excluded the factor of positive or closed margin of the excised vagina, because no patient in this study had this factor.

Histological type was classified as non-keratinizing squamous cell carcinoma, keratinizing squamous cell carcinoma, or adenocarcinoma. Lymphatic vessel infiltration and venous infiltration were individually classified into four grades, from 0 to 3. For tumor width, we measured the largest longitudinal diameter of the tumor. Tumor depth was measured at the area of deepest tumor invasion (Fig. 1). The tumor growth pattern was designated as follows: expansive growth pattern with marked border between the tumor and surrounding tissue was designated as "expansive" infiltrative growth pattern of small or trabecular-like nests of the tumor into interstitial tissue with an unclear border was classified as "invasive", and an intermediate pattern between the above two patterns was classified as "intermediate"

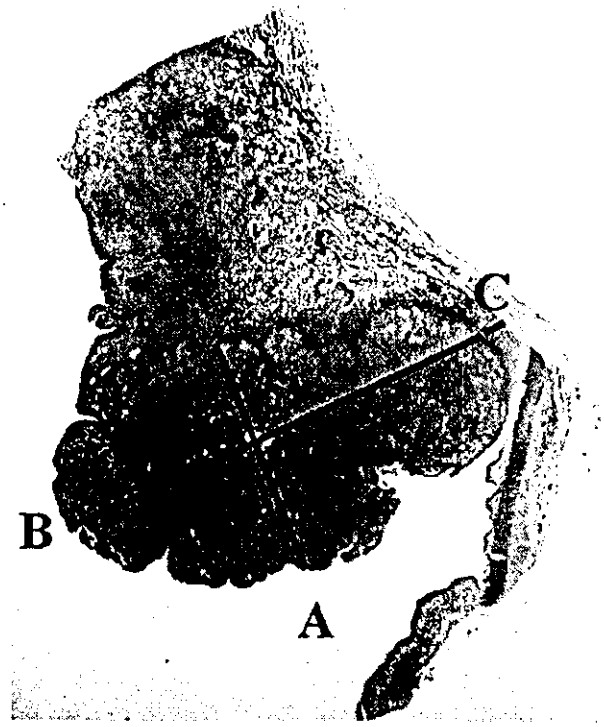

Fig. 1. Measurement of tumor size and residual muscular layer in surgical specimen. *A*, Longitudinal diameter of tumor (tumor width). *B*, Transverse diameter of tumor (tumor depth). *C*, Thickness of the residual normal muscular layer

Follow-up

The follow-up period ranged from 2 to 25 years, with a median of 14 years and 5 months. Recurrence was confirmed pathologically and radiographically. Recurrence in the irradiation field was regarded as local recurrence, and recurrence outside the irradiation field was defined as distant metastases.

Statistical analysis

Overall survival rate (OS), cause-specific survival rate (CSS), and disease-free survival rate (DFS) were analyzed using the Kaplan-Meier method and compared by the log-rank test.[24] Multivariate analysis was performed using the Cox proportional hazard model. Results were considered to be statistically significant when $P < 0.05$. DFS was used as an endpoint for the analysis of prognostic factors. OS was defined as the time from the last date of radiotherapy to

death, CSS as the time from the last date of radiotherapy to death of primary disease, and DFS as the time from the last date of radiotherapy to disease recurrence.

The relationship between the prognostic factors and recurrence patterns was analyzed using the χ^2 test and Fisher's exact probability test.

Risk classification

A risk classification was designed using factors found to be significant. Patients with risk of recurrence were classified based on the number of poor prognostic factors, and the usefulness of the risk classification method was evaluated.

Results

Survival rates and recurrence

Five-year OS, 5-year CSS, and 5-year DFS were 88%, 89%, and 85%, respectively (Fig. 2). There were recurrences in 24 of the 130 patients (18%). Sixteen patients (12%) died of the primary disease. There were local recurrences in 4 patients (3%), distant metastases in other regions in 19 (15%), and multiple recurrences in the irradiation field and distant metastasis in 1 (1%). The time of recurrence ranged from 2 to 174 months, with a median of 16 months. Recurrences occurred within 1 year in 11 patients, 1–5 years in 8, and after 5 years in 5.

Prognostic factors

The details of the statistical analyses of the histopathological prognostic factors are shown in Tables 1 and 2. For univariate analysis, significant differences were observed in six factors: pT factor, venous infiltration, pelvic lymph node metastases, thickness of the residual muscular layer, tumor depth, and tumor growth pattern. For tumor growth pattern, the invasive type was significantly worse than the others. Tumor depth ranged from 2 to 50 mm, and the mean diameter was 13 mm. The prognosis was significantly worse in patients with a 13-mm or larger tumor. The thickness of the residual muscular layer ranged from 0 to 19 mm, and the mean thickness was 5 mm. The prognosis was significantly worse in patients with a 5-mm or thinner muscular layer. On multivariate analysis, venous infiltration was the only significant factor.

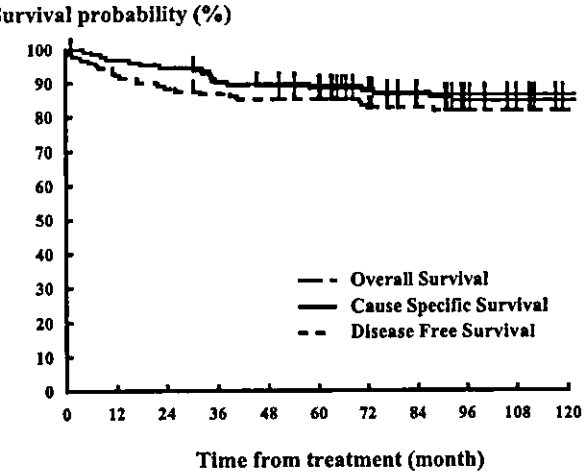

Fig. 2. Survival curves for overall survival, cause-specific survival, and disease-free survival

Recurrence and prognostic factors

The relationship between recurrences and the significant prognostic factors is shown in Table 3. The relationships between the prognostic factors and recurrence patterns were also investigated, but no significant differences were observed.

Risk classification

Risk classification was performed using the six significant prognostic factors. Among the six factors, thickness of the residual muscular layer and tumor depth were correlated with each other, and thus, the thickness of the residual muscular layer was excluded for further analysis. Each of the five factors (parametrial invasion, pelvic lymph node metastases, venous infiltration, tumor growth pattern, and tumor depth) was divided into two categories, 0 or 1. Poor prognosis was defined as 1. All patients were scored, based on the total number of worse categories, using a six-step grade, 0–5. Patients with an overall score of 0–1 were classified as the low-risk group, those with a score of 2 as the intermediate-risk group, and those with a score of 3–5 as the high-risk group (Table 4). The DFS values for the three groups are shown in Fig. 3. Five-year DFS values were 93%, 82%, and 56% in the low; intermediate; and high-risk groups, respectively, showing a significant difference ($P < 0.05$).

Adverse events

Adverse events of radiotherapy were judged according to the National Cancer Institute common toxicity criteria (NCI-CTC). Late adverse events requiring surgery occurred in 6 patients (5%): vesicovaginal fistula in 1, rectovaginal fistula in 1, vesical rupture in 2, ureterostenosis in 1, and intestinal adhesion-induced ileus in 1. These events were judged to be NCI-CTC grade 4. In addition, subileus occurred in 11 patients, hemorrhage that may have been due to radiation enteritis occurred in 4, and lower-limb lymphatic edema occurred in 4, but all these effects were relieved by conservative therapy.

Table 1. Univariate analysis of histopathological prognostic factors

Histopathological factor	No. of patients	5-Year DFS	*P* Value
Histology			
Non-keratinizing-type SCC	82	87%	0.1556
Keratinizing-type SCC	34	88%	
Adenocarcinoma	14	71%	
Pathological extent of tumor			
pT1b	93	88%	0.0149**
pT2a	20	90%	
pT2b	17	64%	
Endometrial invasion			
Negative	100	87%	0.2402
Positive	30	79%	
Vaginal invasion			
Negative	104	85%	0.7980
Positive	26	88%	
Infiltration into lymphatic vessel			
Negative	43	91%	0.1466
Positive	87	83%	
Venous infiltration			
Negative	97	93%	<0.0001*
Positive	33	64%	
Pelvic lymph node metastasis			
Negative	103	90%	0.0003*
Positive	27	70%	
Tumor growth pattern			
Expansive	34	94%	0.0131**
Intermediate	65	85%	
Invasive	31	77%	
Tumor width			
≦27 mm	65	88%	0.3435
>27 mm	65	83%	
Tumor depth			
<13 mm	84	89%	0.0309**
≧13 mm	46	78%	
Remaining muscle layer			
>5 mm	48	94%	0.0202**
≦5 mm	82	80%	

* $P < 0.01$; ** $P < 0.05$
DFS, disease-free survival rate; SCC, squamous cell carcinoma

Table 2. Multivariate analysis of histopathological prognostic factors, using the Cox proportional hazard model

Prognostic factor	95% CI	*P* Value	Relative risk
pT2b	0.344–3.560	0.8642	1.107
Venous infiltration	1.593–10.885	0.0036	4.165
Pelvic LN metastasis	0.834–5.889	0.1106	2.216
Tumor growth pattern (invasive)	0.304–5.582	0.7219	1.302
Tumor depth (≧13 mm)	0.540–4.410	0.4186	1.543
Remaining muscle layer (≦5 mm)	0.380–4.740	0.6465	1.344

Discussion

Clinical outcome

The clinical outcomes of postoperative radiotherapy have been reported to be 72%–90% for 5-year OS and 74%–83% for 5-year DFS.[4,10,15–19] In this study, 5-year OS and DFS were 88% and 85%, respectively, which is comparable to those in the previous reports.

The recurrence rate in this study (24/130; 18%) was similar to previous reports.[4–9] Recurrence occurred within 5 years in 19 patients, but tumors recurred after a more prolonged period in 5 patients. Patients with early-stage cervical cancer may survive for a long period, and sufficient follow-up is necessary.

The frequency of distant metastases after postoperative radiotherapy has been reported to be relatively high in many reports,[6,18,20,21] similar to our study (19/130; 15%). The

Table 3. Relationships between prognostic factors and recurrences

Prognostic factor	All patients (130)		Patients with recurrence (24) Recurrence pattern				
	Absent	Present	PF (4)		DM (19)		PF + DM (1)
			Absent	Present	Absent	Present	Present
Pathological T factor (pT2b)	113	17	4	0	13	6	1
Venous infiltration (positive)	97	33	2	2	7	12	0
Pelvic lymph node metastasis (positive)	103	27	4	0	9	10	1
Tumor growth pattern (invasive)	99	31	2	2	11	8	0
Tumor depth (≧13mm)	84	46	4	0	8	11	1

PF, pelvic failure; DM, distant metastasis

Table 4. Relationship between risk classification and recurrence

	No. of patients	Recurrence	
		+	−
Low	90	7	83
Intermediate	17	5	12
High	23	12	11

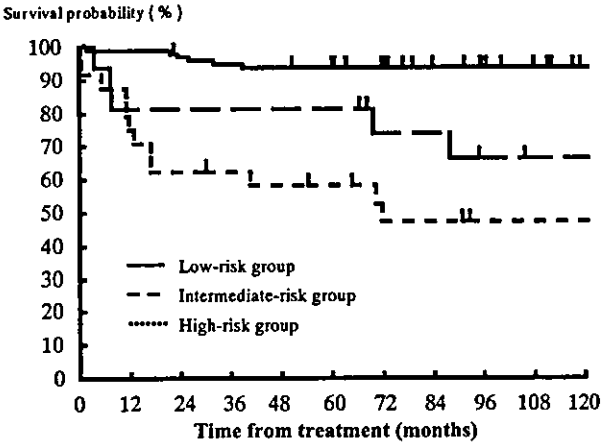

Fig. 3. Disease-free survival for the low-risk, the intermediate-risk, and the high-risk group patients, according to our classification

frequency of local recurrence and distant metastasis was equal,[8,18] or recurrence in the irradiation field was more frequent in previous reports.[16] In this study, the frequency of local recurrence was relatively low (4/130; 3%), while the frequency of distant metastases was 15% (19/130). Postoperative radiotherapy may inhibit local recurrence.

NCI-CTC Grade 4 late adverse events occurred in 6 patients (5%). This frequency was similar to those previously reported.[5,21]

Prognostic factors

Among prognostic factors investigated, pelvic lymph node metastases have been reported as an important prognostic factor in many studies.[3,4,6,7,10–13] Pelvic lymph node metastases were also correlated with recurrence in the present study. However, a significant difference was only observed in the univariate analysis. This factor was not significant in the multivariate analysis. Our analysis was performed only in patients treated with postoperative radiotherapy. The improved survival rate, brought about by pelvic lymphadenectomy and postoperative radiotherapy, for patients with pelvic lymph node metastases, may explain why this prognostic factor was not significant in the multivariate analysis.

Tumor size is regarded as a major prognostic factor in cervical cancer.[22,23] Few reports, however, have mentioned methods of measuring the tumor size. We investigated tumor width and depth individually. Our results showed that tumor depth was a significant prognostic factor. On the other hand, no significant difference was observed for tumor width. The mean tumor depth (13mm) in this study was considerably less than that (40mm) in other reports.[1,4,14,19] We measured the actual transverse diameter of tumors in fixed preparations. Because the tumors had been divided into two parts and fixed in formalin, tumor shrinkage was greater than that in fresh specimens.

For the pT factor, the prognosis was poor only in pT2b patients. The finding of pT2b is synonymous with parametrial invasion, and this factor may have greatly affected the poor prognosis. Parametrial invasion has been reported to be a poor prognostic factor in many studies,[3,4,7,11,12] consistent with our results.

Although vascular infiltration has been reported to be a poor prognostic factor in some reports,[11,12] lymphatic vessel and arterial and venous infiltration were all considered as one factor, "vascular infiltration" in those studies. No study has investigated individual types of vessels, to the best our knowledge. We investigated lymphatic vascular infiltration and venous infiltration individually, and evaluated their significance. Venous infiltration was the most significant prognostic factor, while only a tendency for poor prognosis was observed in patients with lymphatic vessel infiltration. This

finding regarding venous infiltration may be related to the high frequency of distant metastases in those patients with recurrence, but a definite conclusion cannot be made because the number of patients with recurrence was small.

We classified the tumor growth pattern as invasive, intermediate, or expansive type. The prognosis was significantly worse for the invasive type than for the expansive and intermediate types. To our knowledge, there has been no previous study investigating the tumor growth pattern as a prognostic factor.

Risk classification

We also investigated the relationship between the significant prognostic factors and recurrence patterns, but no factor was strongly correlated with the recurrence patterns. It was difficult to judge the risk of recurrence based on a single factor, as multiple factors seemed to be related to each other. To simultaneously investigate multiple factors, we used the risk classification scheme.

Risk classification by scoring prognostic factors has been reported.[13,18,19] Kodaira et al.[19] scored such factors, using three factors based on a Gynecologic Oncology Group (GOG) report[3] (tumor diameter, depth of muscular layer infiltration, and lymphatic-vascular space invasion) in lymph node-negative patients after postoperative irradiation for cervical carcinoma. They divided the patients into low- and high-risk groups, and found that this scoring was useful for the judgment of risk of recurrence. We applied this method to lymph node-negative patients in this study, but no difference was observed between the high-risk and low-risk groups. Aoki et al.[18] scored prognostic factors, using parametrial infiltration and the number of lymph node metastases in lymph node-positive patients after postoperative irradiation for cervical carcinoma. They divided the patients into three risk groups, and obtained useful results. We applied this method to lymph node-positive patients in this study, and a significant difference in risk of recurrence according to scores was observed. However, risk judgment could not be made with their system in lymph node-negative patients, who comprised 79% the population in this study.

The classification we propose is applicable to all patients with cervical cancer treated with radical hysterectomy and postoperative radiotherapy. Our risk classification showed a very high correlation with recurrence.

We used five factors: (1) parametrial invasion, (2) pelvic lymph node metastases, (3) venous infiltration, (4) tumor growth pattern, and (5) tumor depth. These factors are seen in histopathological reports, and therefore clinicians can use this classification routinely. The classification is applicable to all postoperative patients, and is clinically practical.

In addition, the prognosis can be predicted before radiotherapy, because radiotherapy factors are not included. Therefore, using our classification, the selection of more intensive treatment, such as chemoradiotherapy, may be possible.

Conclusion

Significant differences in prognosis were observed for six factors: pT factor, venous infiltration, pelvic lymph node metastases, thickness of the residual muscular layer, tumor depth, and tumor growth pattern. Our risk classification may make it possible to predict which patients are at risk of recurrence.

References

1. Landoni F, Maneo A, Colombo A, et al. (1997) Randomised study of radical surgery versus radiotherapy for stage Ib-IIa cervical cancer. Lancet 350:535–540
2. Japan Society of Obstetrics and Gynecology, The Japanese Society of Pathology, Japan Radiological Society (1997) The general rules for clinical and pathological management of uterine cervical cancer, 2nd edn.
3. Delgado G, Bundy B, Zaino R, et al. (1990) Prospective surgical-pathological study of disease-free interval in patients with stage IB squamous cell carcinoma of the cervix: a Gynecologic Oncology Group Study. Gynecol Oncol 38:352–357
4. Keilholz AS, Hellebrekers BWJ, Zwinderman AH, et al. (1999) Adjuvant radiotherapy following radical hysterectomy for patients with early-stage cervical carcinoma (1984–1996). Radiother Oncol 51:161–167
5. Sedlis A, Bundy BN, Rotman MZ, et al. (1999) A randomized trial of pelvic radiation therapy versus no further therapy in selected patients with stage IB carcinoma of the cervix after radical hysterectomy and pelvic lymphadenectomy: a Gynecologic Oncology Group Study. Gynecol Oncol 73:177–183
6. Chatani M, Nose T, Masaki N, et al. (1998) Adjuvant radiotherapy after radical hysterectomy of the cervical cancer. Strahlenther Onkol 174:504–509
7. Kashihara K, Nishitani H, Takegawa Y, et al. (1992) Clinical evaluation of postoperative radiotherapy for uterine cervical cancer. J Jpn Soc Ther Radiol Oncol 4:45–53
8. Stock RG, Chen ASJ, Flickinger JC, et al. (1995) Node-positive cervical cancer: Impact of pelvic irradiation and patterns of failure. Int J Radiat Oncol Biol Phys 31:31–36
9. Perez CA, Grigsby PW, Camel HM, et al. (1995) Irradiation alone or combined with surgery in stage IB, IIA, and IIB carcinoma of uterine cervix: update of a nonrandomized comparison. Int J Radiat Oncol Biol Phys 31:703–716
10. Yeh SH, Leung SW, Wang CJ, et al. (1999) Postoperative radiotherapy in early stage carcinoma of the uterine cervix: treatment results and prognostic factors. Gynecol Oncol 72:10–15
11. Gonzalez DG, Ketting BW, van Bunningen B, et al. (1989) Carcinoma of the uterine cervix stage IB and IIA: results of post operative irradiation in patients with microscopic infiltration in the parametrium and/or lymph node metastasis. Int J Radiat Oncol Biol Phys 16:389–395
12. Kamura T, Tsukamoto N, Tsuruchi N, et al. (1993) Histopathologic prognostic factors in stage IIB cervical carcinoma treated with radical hysterectomy and pelvic-node dissection – an analysis with mathematical. Int J Gynecol Cancer 3:219–225
13. Gauthier P, Gore I, Shingleton HM, et al. (1985) Identification of histopathologic risk groups in stage Ib squamous cell carcinoma of the cervix. Obstet Gynecol 66:569–574
14. Tsai CS, Lai CH, Wang CC, et al. (1999) The prognostic factors for patients with early cervical cancer treated by radical hysterectomy and postoperative radiotherapy. Gynecol Oncol 75:328–333
15. Lai CH, Hong JH, Hsueh S, et al. (1999) Preoperative prognostic variables and the impact of postoperative adjuvant therapy on the outcomes of stage IB or II cervical carcinoma patients with or without pelvic lymph node metastases: an analysis of 891 cases. Cancer 85: 1537–1546